J. Non-Newtonian Fluid Mech. 165 (2010) 743–751

Contents lists available at ScienceDirect

Journal of Non-Newtonian Fluid Mechanics

journal homepage: www.elsevier.com/locate/jnnfm

Purely elastic instabilities in three-dimensional cross-slot geometries

A.M. Afonso[a], M.A. Alves[a], F.T. Pinho[b,*]

[a] Faculdade de Engenharia da Universidade do Porto, Dep. Eng. Química, CEFT, 4200-465 Porto, Portugal
[b] CEFT, Dep. Eng. Mecânica, Faculdade de Engenharia da Universidade do Porto, 4200-465 Porto, Portugal

ARTICLE INFO

Article history:
Received 22 January 2010
Received in revised form 28 March 2010
Accepted 29 March 2010

Keywords:
3D cross-slot
Elastic instability
UCM model
Flow bifurcation
Finite-volume method

ABSTRACT

Creeping and low Reynolds number flows of an upper-convected Maxwell (UCM) fluid are investigated numerically in a three-dimensional orthogonal cross-slot geometry. We analyze two different flow configurations corresponding to uniaxial extension and biaxial extension, and assess the effects of extensional flow type, Deborah and Reynolds numbers on flow dynamics near the interior stagnation point. Using these two flow arrangements the amount of stretch and compression near the stagnation point can be varied, providing further insights on the viscoelastic flow instability mechanisms in extensionally dominated flows with an interior stagnation point. The uniaxial extensional flow arrangement leads to the onset of a steady flow asymmetry, followed by a second purely elastic flow instability that generates an unsteady flow at higher flow rates. On the other hand, for the biaxial extension flow configuration a symmetric flow is observed up to the critical Deborah number when the time-dependent purely elastic instability sets in, without going through the steady symmetric to steady asymmetric transition.

1. Introduction

The occurrence of purely elastic instabilities in several canonical viscoelastic fluid flows is now a recognized fact. These instabilities are often present in extensionally dominated viscoelastic flows containing an interior stagnation point, such as the opposed jet device [1], the four-roll mill apparatus [2] and the cross-slot geometry [3,4]. Purely elastic instabilities have also been observed in shear flows with or without extensional flow contributions. Examples of the former are found in the flow in the mixing–separating geometry investigated by Afonso et al. [5] and in converging flows in abrupt contractions [6] or in T-like geometries [7,8]. The Taylor–Couette instability is an example of a shear flow without extensional flow contributions in which elastic instabilities arise [9,10], but other shear flows with streamline curvature also originate elastic instabilities [11], which can eventually lead to elastic turbulence as argued by Groisman and Steinberg [12], and provided the instability threshold is independent of the wave number. These pure shear flows of viscoelastic fluids with streamline curvature are linearly unstable, as quantified by various criteria [9,13], and summarized by the Pakdel–McKinley criterion [11]. Theoretical modeling of extension dominated flows and its instabilities and singularities have also been extensively investigated, as in the works of Rallison and Hinch [14], Renardy [15], Thomases and Shelley [16] and Becherer et al. [17]. These flows have received particular attention recently due to their potential use in the measurement of the extensional viscosity of dilute polymer solutions in micro systems, where the elastic nature of the fluid is amplified by the small scales [18].

Of particular relevance to this study is the experimental observation of instabilities in a "quasi two-dimensional" cross-slot microchannel flow by Arratia et al. [3] (this cross-slot is bounded by flat top and bottom walls), which motivated the numerical work by Poole et al. [4] on the two-dimensional cross-slot flow of an upper-convected Maxwell (UCM) fluid under low Reynolds number flow conditions. These authors were able to predict the onset of a bistable steady asymmetric flow above a critical Deborah number (*De*), followed by a second transition to a time-dependent flow at higher *De*. These numerical results were qualitatively in agreement with the experimental observations of the quasi two-dimensional flow of Arratia et al. [3]. Subsequently, Poole et al. [19] considered the true three-dimensional nature of a real microfluidic cross-slot flow and investigated the effect of the aspect ratio of the geometry, by varying the depth of the slot channel from a quasi-Hele-Shaw flow configuration up to large aspect ratios (quasi-2D flow). Later, Poole et al. [20] incorporated the effect of solvent viscosity ($\beta \neq 0$ in the Oldroyd-B model) and finite extensibility ($\varepsilon \neq 0$ in the sPTT model), presenting β–*Re*–*De* and ε–*Re*–*De* maps of flow pattern types, showing the existence of a narrow region where steady asymmetric flow can emerge, and identified the limiting *De* for onset of time-dependent flow. The effect of finite extensibility was also studied numerically by Rocha et al. [21] and analytically by Becherer et al. [17], using FENE models.

In this work the previous investigations for planar geometries [4,19,20] are extended to three-dimensional cross-slot flows with

* Corresponding author.
E-mail address: fpinho@fe.up.pt (F.T. Pinho).

0377-0257/$ – see front matter © 2010 Elsevier B.V. All rights reserved.
doi:10.1016/j.jnnfm.2010.03.010

inlets and outlets in the three orthogonal directions. A 3D finite-volume numerical method is used to study the viscoelastic flow inside a 3D six arms cross flow geometry considering two symmetric flow configurations that lead to uniaxial and biaxial extensional flows, respectively. The influence of the ratio of inlet to outlet flow rates and of the Deborah and Reynolds numbers on the onset of the flow instability are investigated numerically in order to demonstrate its purely elastic nature.

The remaining of this paper is organized as follows: in Section 2 we present the governing equations and briefly describe the numerical method used in their solution. Section 3 presents the computational meshes and describes the flow problem under analysis. The numerical results are presented and discussed in Section 4, before ending the paper with the main conclusions of this study.

2. Governing equations and numerical method

The equations to be solved are those of conservation of mass

$$\nabla \cdot \boldsymbol{u} = 0, \tag{1}$$

and momentum

$$\rho \frac{\partial \boldsymbol{u}}{\partial t} + \rho \nabla \cdot \boldsymbol{u}\boldsymbol{u} = -\nabla p + \nabla \cdot \boldsymbol{\tau}, \tag{2}$$

of an incompressible fluid, together with an appropriate constitutive equation for the extra-stress, $\boldsymbol{\tau}$. In this work, for reasons of rheological simplicity, the UCM model is used

$$\boldsymbol{\tau} + \lambda \left(\frac{\partial \boldsymbol{\tau}}{\partial t} + \nabla \cdot \boldsymbol{u}\boldsymbol{\tau} \right) = \eta \left(\nabla \boldsymbol{u} + \nabla \boldsymbol{u}^{\mathrm{T}} \right) + \lambda \left(\boldsymbol{\tau} \cdot \nabla \boldsymbol{u} + \nabla \boldsymbol{u}^{\mathrm{T}} \cdot \boldsymbol{\tau} \right), \tag{3}$$

where λ and η are the relaxation time and shear viscosity of the fluid, respectively. An alternative formulation of this constitutive law writes the extra-stress tensor as an explicit function of the conformation tensor **A**, which for the UCM model reads as,

$$\boldsymbol{\tau} = \frac{\eta_p}{\lambda} (\boldsymbol{A} - \boldsymbol{I}). \tag{4}$$

Then, the conformation tensor **A** is described by an evolution equation which for the UCM is

$$\lambda \left(\frac{\mathrm{D}\boldsymbol{A}}{\mathrm{D}t} - \nabla \boldsymbol{u} \cdot \boldsymbol{A} - \boldsymbol{A} \cdot \nabla \boldsymbol{u}^{\mathrm{T}} \right) = (\boldsymbol{A} - \boldsymbol{I}). \tag{5}$$

The main advantage of this transformation is on its numerical solution since it provides the possibility of using the log-conformation technique, introduced by Fattal and Kupferman [22], which has been shown to lead to a significant increase of numerical stability [23–27]. In this technique a simple tensor-logarithmic transformation is performed on the conformation tensor for differential viscoelastic constitutive equations. This technique can be applied to a wide variety of constitutive laws and in the log-conformation representation the evolution equation (5) is replaced by an equivalent evolution equation for the logarithm of the conformation tensor, $\boldsymbol{\Theta} = \log \boldsymbol{A}$, benefiting from the fact that **A** is a symmetric positive definite matrix, and thus can be diagonalized into the form [22]

$$\boldsymbol{A} = \boldsymbol{O}\boldsymbol{X}\boldsymbol{O}^{T}, \tag{6}$$

where **O** is an orthogonal matrix generated with the eigenvectors of matrix **A** and **X** is a diagonal matrix created with the corresponding three distinct eigenvalues of **A**. The transformation from equation (5) to an equation for $\boldsymbol{\Theta}$ is described by Fattal and Kupferman [22], and leads to

$$\frac{\partial \boldsymbol{\Theta}}{\partial t} + (\boldsymbol{u} \cdot \nabla)\boldsymbol{\Theta} - \left(\boldsymbol{R}\boldsymbol{\Theta} - \boldsymbol{\Theta}\boldsymbol{R} \right) - 2\boldsymbol{E} = \frac{1}{\lambda} \left(e^{-\boldsymbol{\Theta}} - \boldsymbol{I} \right). \tag{7}$$

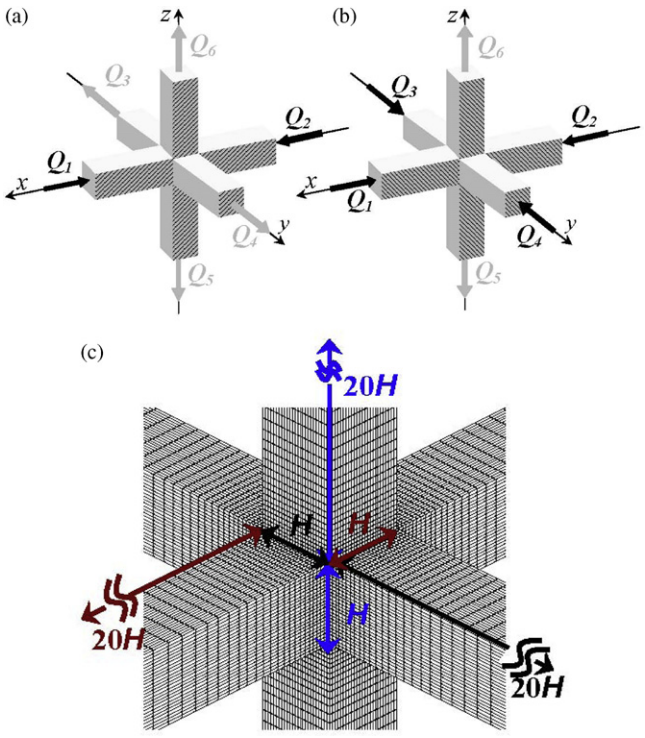

Fig. 1. Schematic view of the cross-slot geometry: (a) biaxial extension configuration (I_o = 2:4); (b) uniaxial extension configuration (I_o = 4:2) and (c) zoomed view of the mesh near the center.

In Eq. (7) **R** and **E** are a pure rotational tensor and a traceless extensional tensor, respectively, which combine to form the velocity gradient tensor [22]. To recover **A** from $\boldsymbol{\Theta}$ the inverse transformation $\boldsymbol{A} = \mathrm{e}^{\boldsymbol{\Theta}}$ is used when necessary. The extra-stress tensor can be obtained, if necessary, using Eq. (4).

A fully implicit finite-volume method (FVM) was used to solve Eqs. (1)–(7). This fully implicit FVM is based on a time marching pressure-correction algorithm and is formulated with the collocated variable arrangement. The numerical method used to solve the log-conformation evolution equation is explained in detail in Afonso et al. [26] and in some references therein. The advective terms were discretized with the CUBISTA high-resolution scheme [28], formally of third-order accuracy. Along with inertial effects, in this work we will also focus on creeping-flow conditions (Re = 0), in which case the advective term in the momentum equation is neglected.

3. Flow problem and computational meshes

The three-dimensional cross-slot geometry is illustrated in Fig. 1, for the two flow configurations studied in this work. The geometries are identified by the ratio of the number of inlets to the number of outlets (I_o): the biaxial extension configuration (I_o = 2:4) has two inlets (Q_1 and Q_2) and four outlets (Q_3–Q_6) and the uniaxial extension configuration (I_o = 4:2) has four inlets (Q_1–Q_4) and two outlets (Q_5 and Q_6).

These configurations generate different degrees of stretch and compression near the stagnation point, providing new insights into the viscoelastic flow instability mechanism in cross-slot flows. For the coordinate system illustrated in Fig. 1, and using the definition of strain rate tensor [29], its components at the stagnation point

are given by

$$\dot{\varepsilon}_{ij} = \dot{\varepsilon}_0 \begin{bmatrix} -(m+1) & 0 & 0 \\ 0 & m & 0 \\ 0 & 0 & 1 \end{bmatrix} \tag{8}$$

Depending on the value of the parameter m, different types of extensional flow can be observed near the interior stagnation point. For the biaxial extension configuration ($I_o = 2{:}4$), represented in Fig. 1**a**, $m = 1$, while for the uniaxial extension configuration ($I_o = 4{:}2$), sketched in Fig. 1**b**, $m = -1/2$. In general, for extensional flows m is in the range $-1/2 \le m \le 1$.

The central region of the cross-slot, corresponding to the intersection of the six arms, defines a cube with side length H. The length of the inlet and outlet "arms" is $L = 20\,H$. Fully developed velocity (with an average value U) and stress profiles are imposed as inlet boundary conditions, while at outlets Neumann boundary conditions are imposed to all variables, i.e. $\partial\varphi/\partial x = 0$, including the pressure gradient. Previous works for 2D flow [4,19,20] confirm that further increases in the inlet and outlet arms lengths have a negligible effect on the critical Deborah number for elastic instabilities and on the flow patterns. The Deborah number is here defined as $De = \lambda U/H$ and the Reynolds number as $Re = \rho UH/\eta$.

The mesh used in the numerical simulations has a total of 203,125 cells, corresponding to 2,031,250 degrees of freedom. A zoomed view of the mesh at the central region of the cross-slot is also presented in Fig. 1c, along with a description of relevant dimensions. The central cubic region of the cross-slot has 25 cells along each direction (x, y and z), corresponding to minimum cell sizes of $\Delta x_{\min}/H = \Delta y_{\min}/H = \Delta z_{\min}/H = 0.04$. Increasing the mesh refinement leads to significant increases in the CPU times, due to the three-dimensional nature of the flow, therefore more detailed three-dimensional mesh refinement studies will be undertaken in the future. For this particular mesh, we can estimate the numerical uncertainty of the results to be less then 5% from the investigation of the corresponding 2D flows [7,21], where extensive mesh refinement studies were carried out. These three-dimensional simulations were carried out in a AMD dual core with 2 GHz and 2 GB of RAM and each complete simulation for steady state flow conditions took on average from 12 to 24 h of CPU time at low De, going up to about 340 h of CPU time at the highest De, where the flow is asymmetric.

4. Results

Due to the complex three-dimensional flow dynamics it is more difficult to quantify the flow asymmetry than for two-dimensional flows. For that purpose we used the main direction angles of the rate of deformation tensor at the interior stagnation point. To obtain such angles we decomposed the deformation rate tensor,

$$\boldsymbol{D} = \frac{1}{2}\left[\nabla \boldsymbol{u} + (\nabla \boldsymbol{u})^{\mathrm{T}}\right], \tag{9}$$

into its eigenvalues and corresponding right eigenvectors,

$$\boldsymbol{D}\boldsymbol{v}_i = \lambda_i \boldsymbol{v}_i \quad i = 1, 2, 3 \quad (\text{no summation on } i). \tag{10}$$

The eigenvectors $\boldsymbol{v_1}$, $\boldsymbol{v_2}$, and $\boldsymbol{v_3}$ are the principal directions of the deformation rate tensor, i.e. the shear-free directions, and the corresponding eigenvalues λ_1, λ_2, and λ_3 are the principal strain rates, thus quantifying the elongations in the principal directions. Finally, we define the *direction angles* as the angles between the principal directions of the deformation rate tensor and the versors that define the coordinate system ($\hat{\boldsymbol{e}}_j$), $\kappa_{ij} = \arccos(\boldsymbol{v}_i \cdot \hat{\boldsymbol{e}}_j / \left\|\boldsymbol{v}_i\right\|)$ (no summation over identical indices). In particular, we are interested in determining the *main direction angles*, which are obtained when $i = j$.

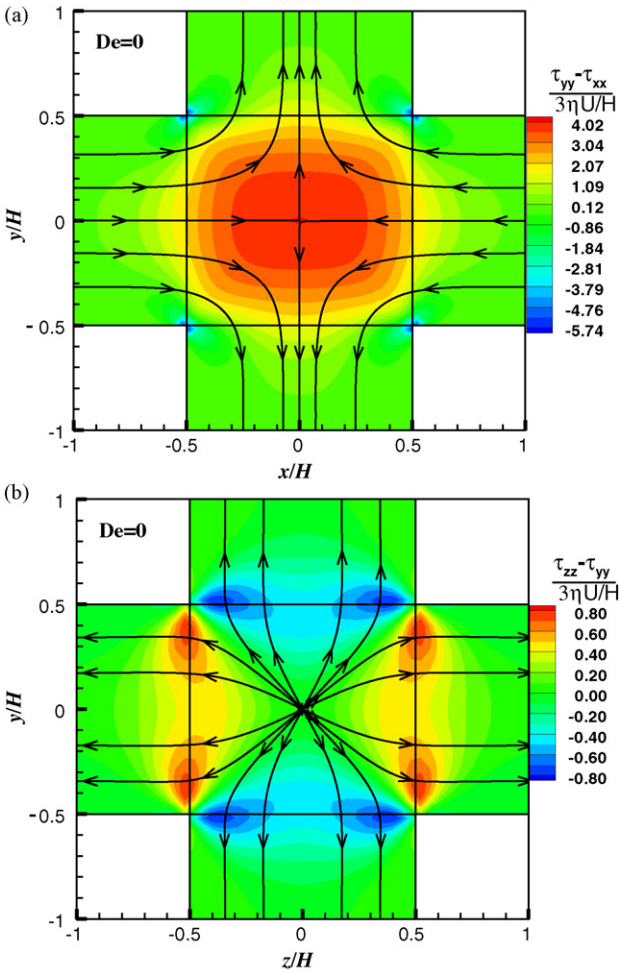

Fig. 2. Flow patterns and contour plots of normalized first normal-stress differences for Newtonian flow for $I_o = 2{:}4$ at centre planes (a) xy and (b) yz.

Results are presented in Section 4.1 for the flow in the biaxial extension configuration ($I_o = 2{:}4$) and in Section 4.2 for uniaxial extensional flow ($I_o = 4{:}2$).

4.1. Biaxial extension configuration ($I_o = 2{:}4$)

The creeping-flow simulations for the biaxial extension flow ($I_o = 2{:}4$) did not present any signs of asymmetry up to $De \approx 0.61$. The principal angle directions calculated in the vicinity of the central stagnation point, show that the three κ_{ii} remain constant with the increase of the Deborah numbers up to $De \approx 0.61$, with $\kappa_{11} = 0$ and $\kappa_{22} = \kappa_{33} = \pi/4$. Under these conditions the flow is shear free in this central region as can be observed in Figs. 2 and 3, where the flow characteristics are shown via stream traces and contour plots of normalized normal-stress differences, $\left(\tau_{jj} - \tau_{ii}\right) / \left(3\eta U/H\right)$, for Newtonian and $De = 0.6$ flows, respectively (no summation over repeated indices and $i \neq j$). It is clear that the flow remains symmetric for these two cases. At $De \approx 0.3$ we start to observe the appearance of symptoms of *diverging streamlines* [30] in the yz centreplane, the plane where the strain rate is positive, but the flow remains symmetric in relation to all planes (no change in κ_{ii}). The *diverging streamlines* phenomenon is seen when we also observe the waved stream traces near the corners of the two exit ducts, especially at higher De, as shown in Fig. 3(b). Then, above a critical Deborah number, $De = 0.62$, the flow becomes unsteady, with oscillations occurring in all directions. Thus, in the biaxial extension flow, the first transition is directly from a steady symmetric flow

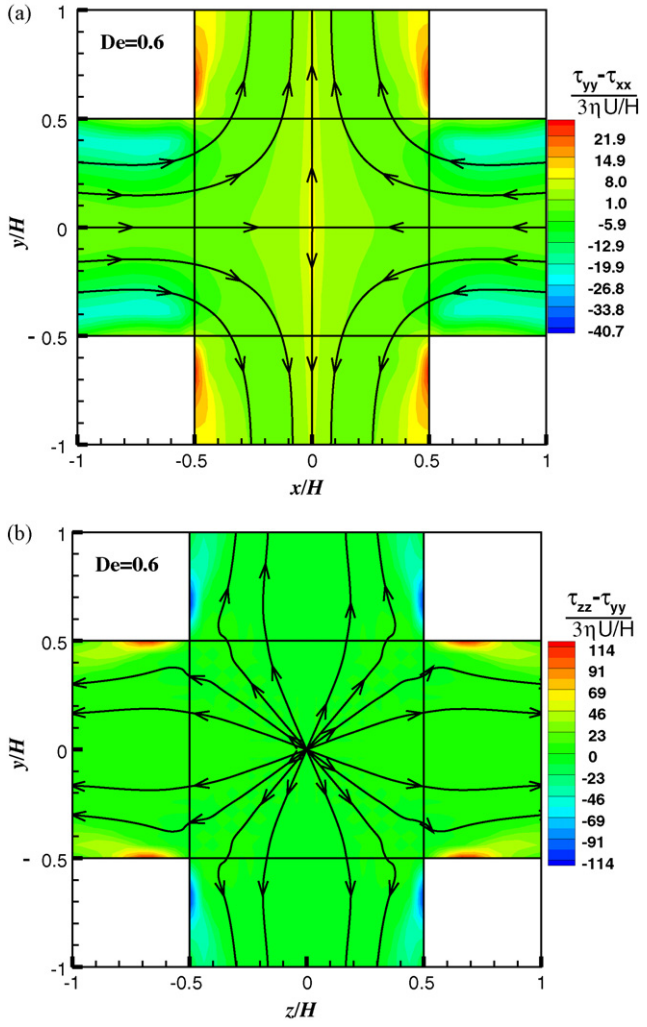

Fig. 3. Flow patterns and normalized first normal-stress differences contours at $De = 0.6$ for $I_o = 2{:}4$ at planes (a) *xy* and (b) *yz*.

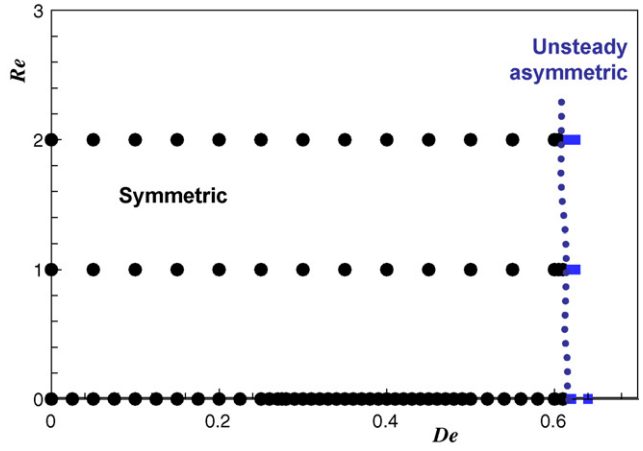

Fig. 4. *Re–De* stability map for the biaxial extension flow configuration ($I_o = 2{:}4$).

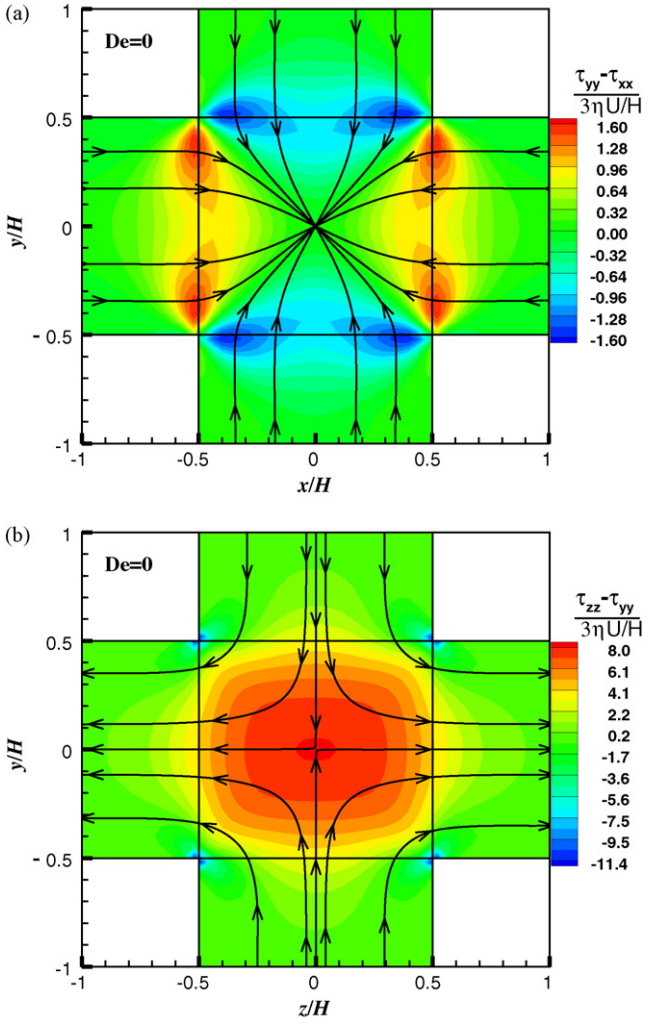

Fig. 5. Flow patterns and contour plots of normal-stress differences for Newtonian flow for $I_o = 4{:}2$ at centre planes (a) *xy* and (b) *yz*.

to a time-dependent flow, not showing the intermediate regime of a bi-stable steady asymmetric flow, as reported by Arratia et al. [3] and Poole et al. [4,19] for a planar cross-slot geometry.

Becherer et al. [17] argued that a transition from a steady to a time-dependent 2D flow in a cross-slot geometry is a purely elastic instability of a highly elastic flow with curved streamlines [11]. However, that referred to a steady asymmetric flow that had previously transitioned from being-extensional dominated to being shear-dominated. This earlier transition has not been observed here in this biaxial extensional flow, which evolves directly from the steady symmetric to an unsteady flow, even though the Reynolds number is zero. So, a question arises as to whether the generalization of Becherer et al. [17] can be extended to any extensional 3D flow or just to uniaxial extension, where there is a transition from steady symmetric to steady asymmetric flow, as will be shown in the next section.

For the biaxial extensional flow ($I_o = 2{:}4$) the effect of inertia is very small for the studied *Re* range [$Re \leq 2$], with the critical Deborah number for the onset of unsteady behavior being nearly constant, as observed in the *Re–De* stability map of Fig. 4, i.e. inertia has a very small destabilizing effect regarding this transition in biaxial extensional flow. Further research into this problem requires the use of finer meshes. For all simulations with $I_o = 2{:}4$, the results in planes *xy* and *xz* were similar.

4.2. Uniaxial extension configuration ($I_o = 4{:}2$)

For the uniaxial extensional flow case ($I_o = 4{:}2$) a transition from steady symmetric flow in all planes (cf. Fig. 5) to a steady asymmetric flow was observed at a rather small critical Deborah number ($De_{crit} \approx 0.22$). Figs. 5 and 6 show the flow patterns and contour

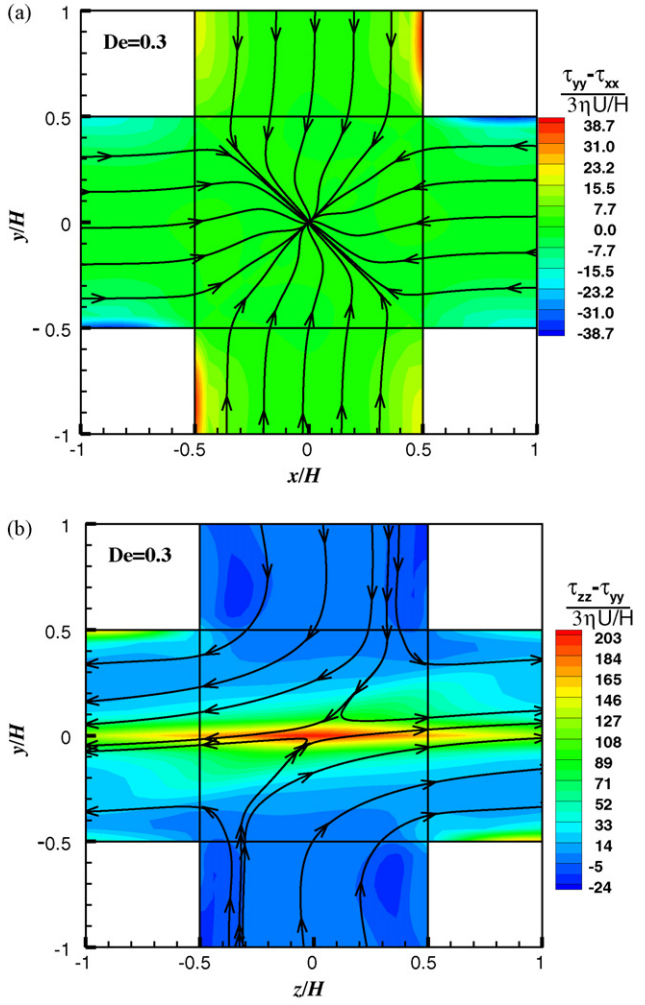

Fig. 6. Projected stream lines at centre planes (a) *xy* and (b) *yz*. Also shown are the contour plots of normal-stress differences for $De = 0.3$ ($I_o = 4{:}2$).

plots of normal-stress differences for $I_o = 4{:}2$ at $De = 0$ and $De = 0.3$ at centre planes *xy* and *yz* (similar to the flow pattern at plane *xz*), respectively. The asymmetric flow is clear with the inlet flow dividing by different amounts into the two *z*-direction channels and in the distortion of the stress contour levels at the centre. We note that in Fig. 6 we are plotting the projected stream lines since the visualized planes are no longer symmetry planes. When the flow is symmetric (as in Fig. 5) the real stream lines are plotted.

When the flow is asymmetric, the flow distortion can be quantified using the main direction angle in the *z*-direction (κ_{33}), as presented in Fig. 7. This clearly shows that an asymmetric flow exists and that the flow at the center is no longer purely extensional, but is a combination of shear and extension. This is more evident in the flow type plots presented in Fig. 8, where the following parameter is used to quantify the local flow type:

$$\xi = \frac{|\boldsymbol{D}| - |\boldsymbol{\Omega}|}{|\boldsymbol{D}| + |\boldsymbol{\Omega}|}, \tag{11}$$

where $|\boldsymbol{D}|$ and $|\boldsymbol{\Omega}|$ represent the magnitudes of the rate of deformation tensor – Eq. (9) – and vorticity tensor,

$$\boldsymbol{\Omega} = \frac{1}{2}\left[\nabla \boldsymbol{u} - (\nabla \boldsymbol{u})^{\mathrm{T}}\right], \tag{12}$$

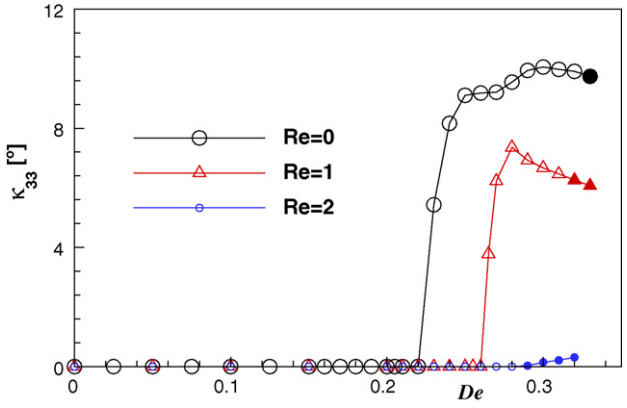

Fig. 7. Variation of main direction angle κ_{33} with Deborah number at the center of the cross-slot for uniaxial extension flow ($I_o = 4{:}2$). Full symbols represent unsteady simulations.

which can be calculated as

$$|\boldsymbol{D}| = \sqrt{\frac{1}{2}\left(\boldsymbol{D} : \boldsymbol{D}^{\mathrm{T}}\right)} = \sqrt{\frac{1}{2}\sum_i\sum_j D_{ij}^2};$$

$$|\boldsymbol{\Omega}| = \sqrt{\frac{1}{2}\left(\boldsymbol{\Omega} : \boldsymbol{\Omega}^{\mathrm{T}}\right)} = \sqrt{\frac{1}{2}\sum_i\sum_j \Omega_{ij}^2}. \tag{13}$$

This flow type parameter has previously been used by Lee et al. [31] and Mitsoulis and Hatzikiriakos [32] and apparently much earlier by Fuller and Leal [33], amongst others.

The flow type parameter varies from $\xi = -1$, which corresponds to solid-like rotation, up to $\xi = 1$, which corresponds to extensional flow. A shear flow is identified when $\xi \to 0$. As observed in Fig. 8, for the Newtonian fluid the flow in the central part of the geometry is essentially of extensional nature, except near the walls where the expected shear flow is observed. On the other hand, for $De = 0.3$ we can observe an important shear region near the stagnation point, thus showing that the transition to asymmetric flow is accompanied by a flow type transition, from an extensionally dominated flow to a situation where shear effects become dominant. In order to better understand this transition, we plot in Fig. 9 the variation with *De* of the local Weissenberg number, $Wi = \lambda\dot{\varepsilon}$, calculated at the stagnation point. The strain rate at the stagnation point can be calculated from the second and third invariants of the rate of deformation tensor [29,34],

$$\dot{\varepsilon} = 3\frac{I_3(\boldsymbol{D})}{I_2(\boldsymbol{D})} = \frac{6\ \det(\boldsymbol{D})}{\mathrm{tr}(\boldsymbol{D}^2)}. \tag{14}$$

As observed in Fig. 9, for low Deborah numbers ($De < 0.05$) there is a linear relation between *Wi* and *De*. As the coil stretch transition is approached ($Wi = 0.5$) *Wi* tends to a plateau. We note, however, that for $De > 0.1$ the local Weissenberg number at the stagnation point exceeds the critical value ($Wi = 0.5$) and the stream wise normal stress becomes unbounded. As also found for the planar cross-slot flow, it is not the unbounded nature of the normal stress at the stagnation point that drives the first instability [4]. Indeed, for the planar cross-slot this instability is also observed with models that have bounded extensional viscosities, such as the FENE-CR model used by Rocha et al. [21]. However, until the critical *De*, the local Weissenberg number at the stagnation point does not increase further, otherwise the singularity of the normal-stress field would become more severe [17]. When the asymmetric flow sets in, we observe a significant decrease of ξ at the stagnation point, with a transition to a shear-dominated flow, as also shown in Fig. 9.

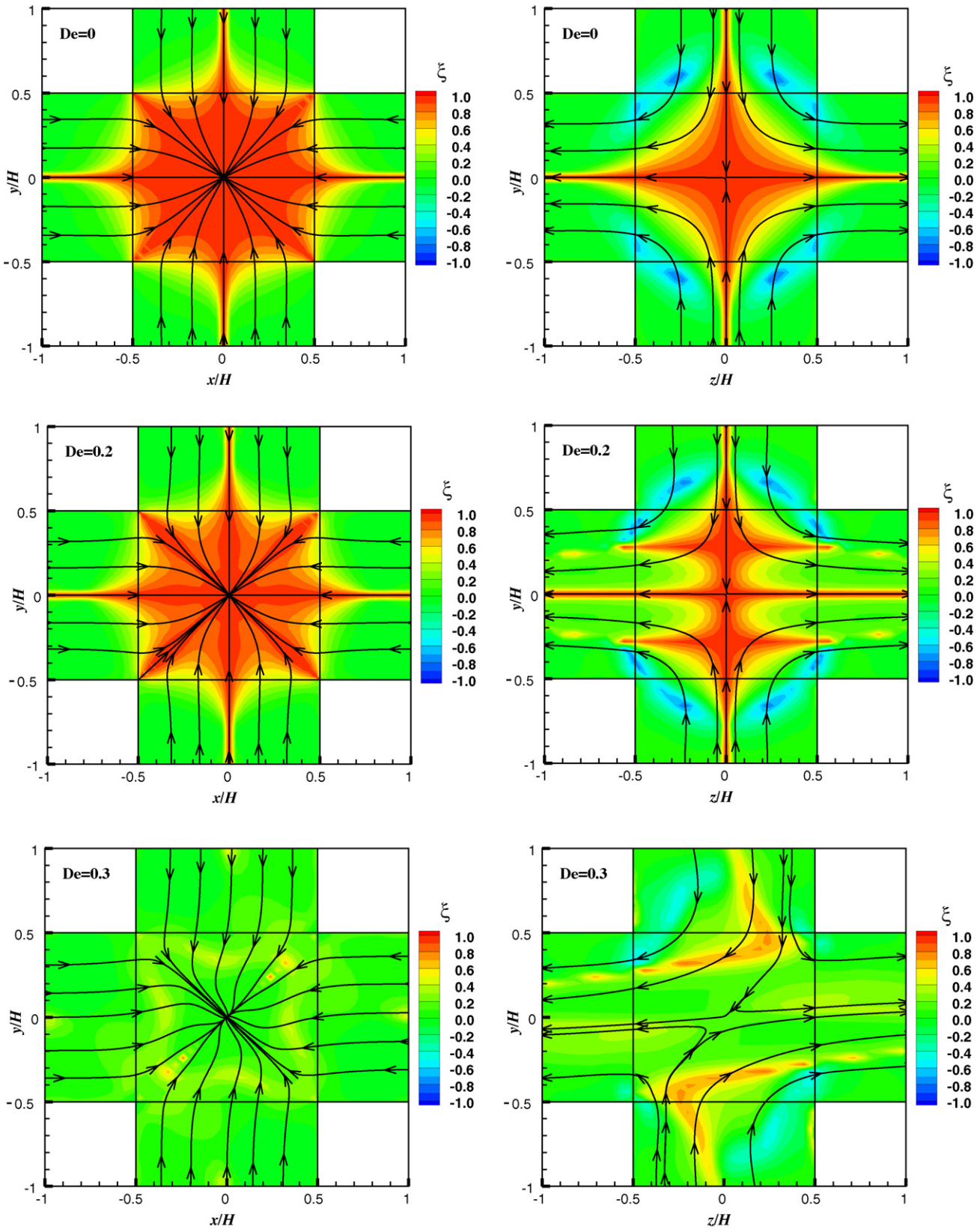

Fig. 8. Flow type parameter and projected stream lines at centre planes *xy* and *yz* for *De* = 0, 0.2 and 0.3.

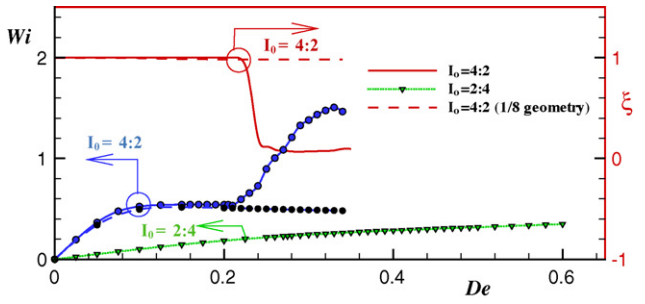

Fig. 9. Variation with *De* of the local Weissenberg number (*Wi*) and flow type parameter (ξ) at the stagnation point for the biaxial (I_o = 2:4) and uniaxial (I_o = 4:2) extensional flow configurations. Values for the symmetry-imposed flow also included for the uniaxial configuration.

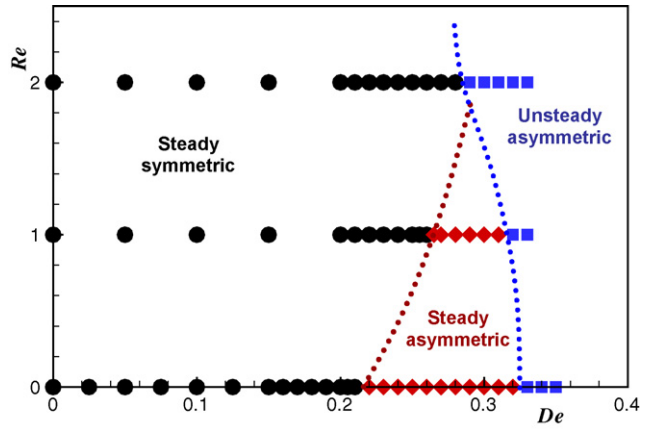

Fig. 10. *Re–De* stability map for the uniaxial extension configuration (I_o = 4:2).

Becherer et al. [17] analytically studied the effect of the boundary conditions for the normal and shear components of the stress tensor at the inflow boundaries of the central region of the cross-slot flow geometry. The authors argued that the first instability observed in the cross-slot geometry [3,4,19] corresponds to a switching from elongational-dominated to shear-dominated velocity field, whereas the second transition is that of a shear-dominated flow with curved streamlines, in agreement with the present results. In Fig. 9 we also plot the variation of *Wi* at the stagnation point with *De* for the biaxial extension configuration (I_o = 2:4), and it is clear that the asymmetric steady flow configuration is not observed because of the lower *Wi* values attained before the onset of the unsteady instability. Presumably, for the I_o = 2:4 configuration when the extensional flow becomes unstable any asymmetric steady shear flow is inherently unstable and the transition is directly from steady extensional to unsteady flow.

We have also undertaken simulations in a geometry consisting of one eighth of the full domain (for I_o = 4:2), and imposing symmetry at the geometric *xy*, *xz* and *yz* symmetry planes crossing the origin of the Cartesian system of coordinates. For lower Deborah number conditions ($De < De_C$) the results with the full geometry and the geometry with imposed symmetry coincide. However, above the critical *De* the artificially imposed symmetry will be representative of the flow field that would be obtained if there was no perturbation in the flow that drives the asymmetry. As shown in Fig. 9, in this case the flow at the stagnation point is still extensionally dominated ($\xi \approx 1$), in contrast with the full mesh simulations where the transition to a quasi shear flow is observed, with a simultaneous increase of the local deformation rate.

Further increasing the Deborah number leads to a second flow transition from a steady asymmetric flow to an unsteady asymmetric flow as in the experiments of Arratia et al. [3] and in the 2D numerical works of Poole et al. [4,19] for "quasi 2D" and 2D cross-slot flows, respectively. This is seen in the stability map of Fig. 10 for *Re* = 0, where the two Deborah numbers for the first and second transitions are approximately 0.22 and 0.32, respectively.

Regarding the effect of flow inertia, the trends are different for the first and second transitions: whereas inertia has a stabilizing effect for the first transition from steady symmetric to steady asymmetric flow (the first critical Deborah number increases with *Re*), for the second transition from steady asymmetric to unsteady flow inertia helps destabilize the flow and the second Deborah number decreases with *Re,* as is also observed for the transition in the I_o = 2:4 flow configuration, although to a much lesser degree. Hence, at *Re* = 0, the second transition takes place at $De_{crt} \approx 0.32$, for *Re* = 1 $De_{crt} \approx 0.31$ and at *Re* = 2 $De_{crt} \approx 0.29$. These changes can be observed both in the main direction angle plot (Fig. 7) as well as in the *Re–De* stability map represented in Fig. 10. Finally, for Reynolds numbers in excess of around 2, the transition associated with elasticity is directly from a steady symmetric to an unsteady flow, as is also observed for the transition in the I_o = 2:4 flow configuration for all Reynolds numbers studied. As we have seen above in Figs. 9 and 10, the steady asymmetric flow is predominantly a shear type flow, where transition to unsteady flow is associated with large hoop stresses developing in curved streamlines, as explained by McKinley et al. [11]. In this mechanism the curved streamlines become unstable at hoop stresses that vary inversely with their curvature. Most likely the instability appears first at the curved streamlines near the reentrant corners, but it could also appear elsewhere closer to the stagnation point, where the streamlines are also curved. By raising the Reynolds number the curvature of the streamlines in the region of interest increase and the same critical level of hoop stress is attained at a lower Deborah number. It is easy to visualize that higher inertial forces push the flow towards the central region of the cross-slot and this forces the fluid to turn direction closer to the geometric centre of the cross-slot, thus increasing locally the curvature of the streamlines. It is not so easy to understand on simple terms why there is an increase of streamline curvature with Reynolds number near the reentrant corner, but this possibility is open.

Explaining the stabilizing effect of the Reynolds number for the first transition is more difficult, since we do not even know yet what is the primary cause for the first transition in creeping flow. Even though it is tempting to consider the unbounded stresses as its cause, we suspect that is not the case given the fact that Poole et al. [20], Rocha et al. [21] and Becherer et al. [17] found such transitions to occur for PTT and FENE fluids for the 2D equivalent cross-slot flow. Clearly, understanding the causes of both types of transition in the 2D and 3D cross-slot flows is an important research topic.

As argued by Oliveira et al. [7], the existence of a symmetry-breaking bifurcation is likely to be related with a stress relief mechanism, and this can be assessed by comparing the energy losses in the real flow, with those predicted in the symmetry-imposed flow configuration. For creeping–flow conditions, the power dissipation can be calculated from:

$$\Delta \dot{W}_{real} = \sum_i Q_{in,i} p_{in,i} - \sum_j Q_{out,j} p_{out,j}, \tag{15}$$

where the subscript 'in' refers to inlet boundaries and the subscript 'out' refers to the outflow boundaries. For both flow configurations analyzed in this work one obtains

$$\Delta \dot{W}_{real} = (p_{in} - p_{out}) \sum_i Q_{in,i}. \tag{16}$$

The power dissipation $\Delta \dot{W}_{real}$ can be compared to that of an ideal flow where fully developed shear flow conditions would be

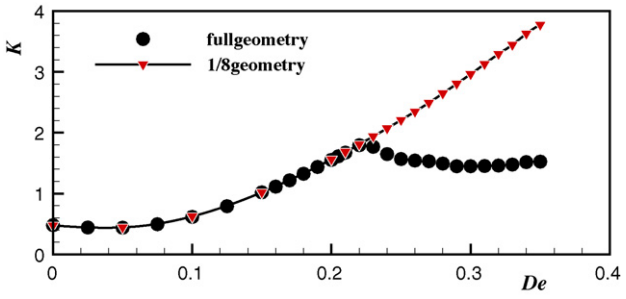

Fig. 11. Effect of Deborah number on the dimensionless extra power dissipation (K) for the uniaxial extension configuration (I_o = 4:2). Simulations with full geometry (●) and 1/8 of the geometry (imposed flow symmetry) (-▽-).

observed everywhere along the channels, and no energy dissipation would take place in the central region of the cross-slot. For this ideal flow configuration the power dissipation can be estimated as

$$\Delta \dot{W}_{\text{ideal}} = \sum_{i=1}^{6} Q_i \left| \mathrm{d}p/\mathrm{d}s \right|_i L_i, \tag{17}$$

where $|\mathrm{d}p/\mathrm{d}s|_i$ represents the absolute value of the stream wise pressure gradient under fully developed flow conditions in arm i. The extra power dissipation due to the extensional flow in the cross-slot geometry can be estimated as (and is independent of the length of the arms, when they are sufficiently long for achieving fully developed flow conditions at inlets and outlets) $\Delta \dot{W}_{\text{exc}} = \Delta \dot{W}_{\text{real}} - \Delta \dot{W}_{\text{ideal}}$. In order to generalize the results, it is useful to work with a dimensionless extra power dissipation, K, here defined as:

$$K = \frac{\Delta \dot{W}_{\text{real}} - \Delta \dot{W}_{\text{ideal}}}{\sum_j Q_{\text{out},j} \left| \mathrm{d}p/\mathrm{d}s \right|_j H} = \frac{\Delta p_{\text{real}} - \Delta p_{\text{ideal}}}{4\tau_{\text{w}}} \tag{18}$$

where Δp_{real} is the pressure difference between one of the inlets and one of the outlets, Δp_{ideal} is the pressure drop required to drive fully developed flow in the inlet and outflow straight channels, as in the absence of the interference of the central region, and τ_{w} is the *average* wall shear stress under fully developed conditions at any of the outflow channels ($\tau_{\text{w}} = \left| \mathrm{d}p/\mathrm{d}s \right|_j H/4$).

In Fig. 11 we present the variation of K with De, together with data from a set of additional calculations with imposed flow symmetry, i.e., simulations with only 1/8 of the geometry. As was also observed in previous works [4,5,7], K is reduced above the critical Deborah number, showing that the steady asymmetric flow dissipates less energy than the symmetric flow configuration. This is an interesting observation, similar to previous works in the planar cross-slot and flow-focusing geometries [4,5,7], but it does not necessarily imply a minimum energy loss principle as the cause for the flow transition.

5. Conclusions

A numerical study of creeping flow of an UCM fluid in three-dimensional cross-slot geometries with six arms was undertaken. The influences of Deborah and Reynolds numbers and different types of extensional flow near the stagnation point were analyzed, namely biaxial and uniaxial extensional flow. The uniaxial extensional flow configuration is prone to the onset of steady flow asymmetries at $De_{\text{crit}} \approx 0.22$ and at a higher Deborah number there is a second transition from steady asymmetric to unsteady flow, as in the corresponding two-dimensional cross-slot geometry. On the other hand, for the biaxial extensional flow configuration a perfectly symmetric flow has been observed up to $De \approx 0.61$ and above this critical Deborah number the flow becomes unsteady and asymmetric without transitioning to a steady asymmetric flow. Inertia was found to stabilize the first type of transition (for the uniaxial extensional flow) and to destabilize the second transition in both flow configurations, although to a much lesser degree in the biaxial extensional flow configuration.

Acknowledgments

The authors acknowledge the financial support from FEDER and FCT through projects PTDC/EQU-FTT/70727/2006, PTDC/EQU-FTT/71800/2006 and scholarship SFRH/BD/28828/2006 (A.M. Afonso).

References

[1] A. Chow, A. Keller, A.J. Müller, A. Odell, Entanglements in polymer solutions under elongational flow: a combined study of chain stretching, flow velocimetry and elongational viscosity, Macromolecules 21 (1988) 250–256.
[2] R.R. Lagnado, N. Phan-Thien, L.G. Leal, The stability of two-dimensional linear flows, Phys. Fluids 27 (1984) 1094–1101.
[3] P.E. Arratia, C.C. Thomas, J.D. Diorio, J.P. Gollub, Elastic instabilities of polymer solutions in cross-channel flow, Phys. Rev. Lett. 96 (2006) 144502.
[4] R.J. Poole, M.A. Alves, P.J. Oliveira, Purely elastic flow asymmetries, Phys. Rev. Lett. 99 (2007) 164503.
[5] A.M. Afonso, M.A. Alves, R.J. Poole, P.J. Oliveira, F.T. Pinho, Viscoelastic flows in mixing separating cells, J. Eng. Mathematics, Submitted for publication.
[6] M.A. Alves, F.T. Pinho, P.J. Oliveira, Viscoelastic flow in a 3D square/square contraction: visualizations and simulations, J. Rheol. 52 (2008) 1347–1368.
[7] M.S.N. Oliveira, F.T. Pinho, R.J. Poole, P.J. Oliveira, M.A. Alves, Purely-elastic flow asymmetries in flow-focusing devices, J. Non-Newt. Fluid Mech. 160 (2009) 31–39.
[8] J. Soulages, M.S.N. Oliveira, P.C. Sousa, M.A. Alves, G.H. McKinley, Investigating the stability of viscoelastic stagnation flows in T-shaped microchannels, J. Non-Newt. Fluid Mech. 163 (2009) 9–24.
[9] R.G. Larson, E.S.G. Shaqfeh, S.J. Muller, A purely elastic instability in Taylor–Couette flow, J. Fluid Mech. 218 (1990) 573–600.
[10] S.J. Muller, E.S.G. Shaqfeh, R.G. Larson, Experimental studies of the onset of oscillatory instability in viscoelastic Taylor-Couette flow, J. Non-Newt. Fluid Mech. 46 (1993) 315–330.
[11] G.H. McKinley, P. Pakdel, A. Öztekin, Geometric and rheological scaling of purely elastic flow instabilities, J. Non-Newt. Fluid Mech. 67 (1996) 19–48.
[12] A. Groisman, V. Steinberg, Elastic turbulence in a polymer solution flow, Nature 405 (2000) 53–55.
[13] Y.L. Joo, E.S.G. Shaqfeh, A purely elastic instability in Dean and Taylor–Dean flow, Phys. Fluids A 4 (1992) 524–543.
[14] J.M. Rallison, E.J. Hinch, Do we understand the physics in the constitutive equation? J. Non-Newt. Fluid Mech. 29 (1988) 37–55.
[15] M. Renardy, A comment on smoothness of viscoelastic stresses, J. Non-Newt. Fluid Mech. 138 (2006) 204–205.
[16] B. Thomases, P. Shelley, Emergence of singular structures in Oldroyd-B fluids, Phys. Fluids 19 (2007) 103103.
[17] P. Becherer, A.N. Morozov, W. van Saarloos, Scaling of singular structures in extensional flow of dilute polymer solutions, J. Non-Newt. Fluid Mech. 153 (2008) 183–190.
[18] T.M. Squires, S.R. Quake, Microfluidics: fluid physics at the nanoliter scale, Rev. Mod. Phys. 7 (2005) 977–1026.
[19] R.J. Poole, M.A. Alves, A. Afonso, F.T. Pinho, P.J. Oliveira, Purely-elastic flow instabilities in a microfluidic cross-slot geometry, in: AIChE 2007 Annual Meeting, 94827, Salt Lake City, 2007.
[20] R.J. Poole, M.A. Alves, A.M. Afonso, F.T. Pinho, P.J. Oliveira, Purely elastic instabilities in a cross-slot flow, in: The Society of Rheology 79th Annual Meeting, Salt Lake City, 2007.
[21] G.N. Rocha, R.J. Poole, M.A. Alves, P.J. Oliveira, On extensibility effects in the cross-slot flow bifurcation, J. Non-Newt. Fluid Mech. 156 (2009) 58–69.
[22] R. Fattal, R. Kupferman, Constitutive laws of the matrix-logarithm of the conformation tensor, J. Non-Newt. Fluid Mech. 123 (2004) 281–285.
[23] Y.D. Kwon, Finite element analysis of planar 4:1 contraction flow with the tensor-logarithmic formulation of differential constitutive equations, Korea-Aust. Rheol. J. 16 (2004) 183–191.
[24] M.A. Hulsen, R. Fattal, R. Kupferman, Flow of viscoelastic fluids past a cylinder at high Weissenberg number: stabilized simulations using matrix logarithms, J. Non-Newt. Fluid Mech. 127 (2005) 27–39.
[25] O.M. Coronado, D. Arora, M. Behr, M. Pasquali, A simple method for simulating general viscoelastic fluid flows with an alternate log-conformation formulation, J. Non-Newt. Fluid Mech. 147 (2007) 189–199.
[26] A.M. Afonso, P.J. Oliveira, F.T. Pinho, M.A. Alves, The log-conformation tensor approach in the finite-volume method framework, J. Non-Newt. Fluid Mech. 157 (2009) 55–65.

[27] A. Kane, R. Guénette, A. Fortin, A comparison of four implementations of the log-conformation formulation for viscoelastic fluid flows, J. Non-Newt. Fluid Mech. 164 (2009) 45–50.
[28] M.A. Alves, P.J. Oliveira, F.T. Pinho, A convergent and universally bounded interpolation scheme for the treatment of advection, Int. J. Numer. Meth. Fluids 41 (2003) 47–75.
[29] R.B. Bird, R.C. Armstrong, O. Hassager, Dynamics of polymeric liquids Fluid Mechanics, vol. 1, 2nd ed., John Wiley & Sons, New York, 1987.
[30] M.A. Alves, R.J. Poole, Divergent flow in contractions, J. Non-Newt. Fluid Mech. 144 (2007) 140–148.
[31] J.S. Lee, R. Dylla-Spears, N-P. Teclemariam, S.J. Muller, Microfluidic four-roll mill for all flow types, Appl. Phys. Lett. 90 (2007) 074103.
[32] E. Mitsoulis, S.G. Hatzikiriakos, Modeling PTFE past extrusion: the effect of an objective flow type parameter, J. Non-Newt. Fluid Mech. 159 (2009) 41.
[33] G.G. Fuller, L.G. Leal, Flow birefringence of dilute polymer solutions in two-dimensional flows, Rheol. Acta 19 (1980) 580.
[34] K. Walters, M.F. Webster, H.R. Tamaddon-Jahromi, The numerical simulation of some contraction flows of highly elastic liquids and their impact on the relevance of the Couette correction in extensional rheology, Chem. Eng. Sci. 64 (2009) 4632–4639.